

PAPER • OPEN ACCESS

## Theoretically optimal turbine resistance in very large wind farms

To cite this article: Alejandro Zapata *et al* 2017 *J. Phys.: Conf. Ser.* **854** 012051

View the [article online](#) for updates and enhancements.

### Recent citations

- [Preliminary estimate of the impact of support structures on the aerodynamic performance of very large wind farms](#)  
Lun Ma and Takafumi Nishino



**IOP | ebooks™**

Bringing you innovative digital publishing with leading voices to create your essential collection of books in STEM research.

Start exploring the collection - download the first chapter of every title for free.

# Theoretically optimal turbine resistance in very large wind farms

Alejandro Zapata, Takafumi Nishino\*, Pierre-Luc Delafin

Cranfield University, Cranfield, Bedfordshire MK43 0AL, United Kingdom

\*E-mail: t.nishino@cranfield.ac.uk

**Abstract.** In this paper we further investigate and validate the novel theoretical model of very large wind farms proposed recently by Nishino (*J. Phys.: Conf. Ser.* 753, 032054, 2016). One of the key features of the Nishino model is that a theoretically optimal turbine resistance (as well as optimal ‘turbine-scale’ and ‘farm-scale’ wind speed reduction rates) can be predicted analytically as a function of the farm density and the natural bottom friction observed before constructing the farm. To validate this theoretical model, a new set of 3D Reynolds-averaged Navier-Stokes (RANS) simulations are performed of a fully developed wind farm boundary layer over an aligned and staggered array of actuator discs with various disc resistance, inter-disc spacing and bottom roughness values. The results show that the theoretical model, which employs only one empirical model parameter, can be easily calibrated to predict very well the performance of various staggered arrays of actuator discs. This suggests the usefulness of the theoretical model not only for providing an upper limit to the performance of ideal large arrays but also for predicting the performance of realistic large arrays. The results also highlight the important fact that the optimal turbine resistance can be significantly smaller in a dense wind farm than in a sparse wind farm.

## 1. Introduction

The size of offshore wind farms has been dramatically increasing in recent years, causing a renewed interest in the modelling of very large wind farms. For example, in 2006, Frandsen et al. [1] reviewed a theoretical model for the interaction between a hypothetical very large wind farm and the planetary boundary layer (PBL), which was developed mainly by Frandsen and Emeis in the 1990’s [2, 3]. Later on, Emeis [4, 5] enhanced the model by considering the effect of atmospheric stability. Calaf et al. [6] also improved the model using results of large-eddy simulations (LES) of a fully developed wind turbine array boundary layer (WTABL). More recently, Meneveau [7] further extended the model by taking into account the development of an internal boundary layer starting from the entrance of a wind farm. This family of theoretical models, which employ the concept of ‘effective wind farm roughness’ and are often referred to as the ‘top-down’ models, predict the reduction of wind speed by a large number of turbines with a given (i.e. empirically known or assumed) thrust coefficient.

Last year, a new type of theoretical model was proposed by Nishino [8] for the performance of a very large wind farm. Similarly to the traditional ‘top-down’ models, this new model also considers a fully developed boundary layer over a very large array of wind turbines. A noteworthy difference, however, is that the turbine thrust coefficient is not arbitrarily given but modelled using the classical (Lanchester-Betz type) actuator disc theory, which allows us to predict a practical upper limit to the efficiency of a very large wind farm together with ‘optimal’ wind speed reduction rates. The validity of this new theoretical model was only partially confirmed in [8]. Therefore in this study, we further



validate this theoretical model by means of a comparison with a series of Reynolds-averaged Navier-Stokes (RANS) simulations of a fully developed boundary layer over an aligned and staggered array of actuator discs, for a range of inter-disc spacing, disc resistance and bottom roughness values.

## 2. Theoretical model

### 2.1. Nishino model

The theoretical model of very large wind farms proposed by Nishino [8] is based on a simple ‘two-scale coupled’ momentum conservation argument. The ‘farm-scale’ wind speed reduction factor,  $\beta$ , is calculated from the momentum balance between the driving force of the atmospheric boundary layer (ABL) and the resistance due to the turbines’ thrust and bottom friction, whereas the ‘turbine-scale’ wind speed reduction factor,  $\alpha$ , is calculated from the classical actuator disc theory. Eventually, these two wind speed reduction factors  $\alpha$  and  $\beta$  satisfy the following momentum conservation equation (see [8] for further details of the derivation):

$$1 - \beta^\gamma = \lambda \cdot \frac{1}{C_{f0}} \cdot \beta^2 \cdot 4\alpha(1 - \alpha) \quad (1)$$

where  $\lambda = A/S$  is the ‘farm density’ (or the ratio of the turbine swept area,  $A$ , to the land area,  $S$ ) and  $C_{f0} = \tau_{w0}/\frac{1}{2}\rho U_{F0}^2$  is the natural friction coefficient defined using the natural wind speed averaged across the so-called ‘farm layer’,  $U_{F0}$ . Note that  $\beta = U_F/U_{F0} (\leq 1)$  is the velocity ratio that indicates how much the farm-layer wind speed changes from its natural state, whereas  $\alpha = U_T/U_F (\leq 1)$  is the ratio of the average wind speed through the turbine swept area to that through the farm layer.

Although this model is essentially one-dimensional (1D; as with the classical actuator disc theory) and there are several possibilities in how to define the height of the farm layer,  $H_F$ , in real three-dimensional (3D) problems, Nishino [8] suggested that  $H_F$  can be defined such that

$$U_{F0} \equiv \frac{\int_0^{H_F} U_0 dz}{H_F} = U_{T0} \equiv \frac{\int U_0 dA}{A} \quad (2)$$

where  $U_0(z)$  is the natural wind speed observed before constructing the wind farm. As will be shown later, this definition of  $H_F$  tends to result in a very good agreement between the 1D theoretical model and 3D RANS simulations of actuator discs.

The only empirical parameter employed in the Nishino model is  $\gamma$  in (1). This parameter describes how the bottom friction (shear stress) changes in response to the reduction of the average wind speed through the farm layer. Specifically,  $\gamma$  is defined such that

$$\frac{\langle \tau_w \rangle}{\tau_{w0}} = \beta^\gamma = \left( \frac{U_F}{U_{F0}} \right)^\gamma \quad (3)$$

where  $\langle \tau_w \rangle$  is the bottom shear stress averaged across the farm. Nishino [8] assumed  $\gamma = 2$  to predict an upper limit to the performance of ‘ideal’ very large wind farms. For ‘real’ very large wind farms, however, the value of  $\gamma$  is expected to be less than 2 since the installation of turbines tends to increase the friction coefficient defined as  $C_f^* = \langle \tau_w \rangle / \frac{1}{2}\rho U_F^2$ . It will be shown later that the  $\gamma$  value in our 3D RANS simulations of actuator discs (for a range of conditions) is around 1.5 to 1.6.

Based on the combination of  $\alpha$  and  $\beta$  that satisfy the momentum conservation equation (1) for a given set of farm parameters  $\lambda$  and  $C_{f0}$  and a given empirical parameter  $\gamma$ , we can calculate the thrust and power coefficients of an ideal turbine (actuator disc) in a very large wind farm as

$$C_T \equiv \frac{\text{Thrust}}{\frac{1}{2}\rho U_{F0}^2 A} = \beta^2 \cdot 4\alpha(1 - \alpha) = \beta^2 \cdot C_T^* \quad (4)$$

and

$$C_P \equiv \frac{\text{Power}}{\frac{1}{2}\rho U_{F0}^3 A} = \beta^3 \cdot 4\alpha^2(1 - \alpha) = \beta^3 \cdot C_P^* \quad (5)$$

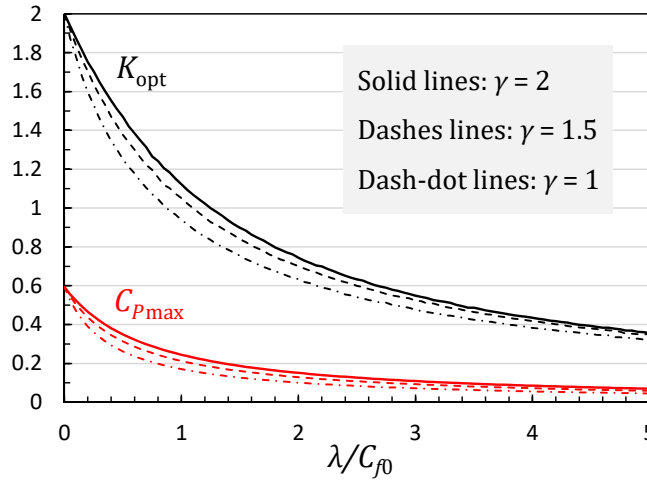


**Figure 1.** Theoretically optimal turbine resistance ( $K_{\text{opt}}$ ) required for ideal turbines (actuator discs) to achieve the maximum power coefficient ( $C_{P\text{max}}$ ) in a very large wind farm.

where  $C_T^*$  and  $C_P^*$  are the ‘local’ or ‘turbine-scale’ thrust and power coefficients that are defined using  $U_F$  instead of  $U_{F0}$ . As demonstrated in [8], this theoretical model allows us to estimate very easily the ‘optimal’ set of wind speed reduction factors ( $\alpha_{\text{opt}}$  and  $\beta_{\text{opt}}$ ) to maximise the power output of a very large wind farm (for a given set of  $\lambda$ ,  $C_{f0}$  and  $\gamma$ ).

### 2.2. Additional notes on the Nishino model

A particularly interesting point here (which was not explicitly mentioned in [8]) is that, since the flow around each turbine has been modelled using the classical actuator disc theory, the ‘turbine-scale’ wind speed reduction rate  $\alpha$  can be further linked to the so-called ‘turbine resistance’  $K$  [9] (which is equivalent to another ‘local’ thrust coefficient  $C_T'$  [6] that is defined using  $U_T$  instead of  $U_F$  or  $U_{F0}$ ). Specifically, the relationship between  $K$  and  $\alpha$  can be described as

$$K = C_T' = \frac{C_T^*}{\alpha^2} = \frac{4(1-\alpha)}{\alpha} \quad (6)$$

This means that the Nishino model also allows us to estimate an ‘optimal’ turbine resistance ( $K_{\text{opt}}$ ) to maximise the power of a very large wind farm (for a given set of  $\lambda$ ,  $C_{f0}$  and  $\gamma$ ) as shown in Figure 1. As can be seen from the figure, the optimal turbine resistance decreases exponentially as the value of  $\lambda/C_{f0}$  increases (i.e. as the farm density increases relative to the natural friction coefficient).

## 3. RANS simulations

### 3.1. Geometry and flow conditions

Similarly to [6] and [8], for all simulations in this paper, a boundary-layer flow driven by a constant streamwise pressure gradient is considered over an ‘infinitely large’ wind farm. This ‘infinitely large’ farm is modelled as a doubly periodic array of actuator discs. Only one disc is placed in the middle of a relatively small (but periodic) rectangular computational domain since we employ (steady) RANS simulations instead of LES.

For all simulation cases, the disk diameter,  $D$ , is 100m. The disc is located at the centre of the domain with a vertical gap between the disc edge and the ground (bottom boundary) of  $0.5D$ . The height of the computational domain,  $L_y$ , is fixed at  $10D$  for all cases, whereas a square horizontal section of either  $(L_x, L_z) = (6D, 6D)$ ,  $(7D, 7D)$  or  $(14D, 14D)$  is employed, i.e. always keeping the streamwise ( $L_x$ ) and spanwise ( $L_z$ ) dimensions of the domain equal.

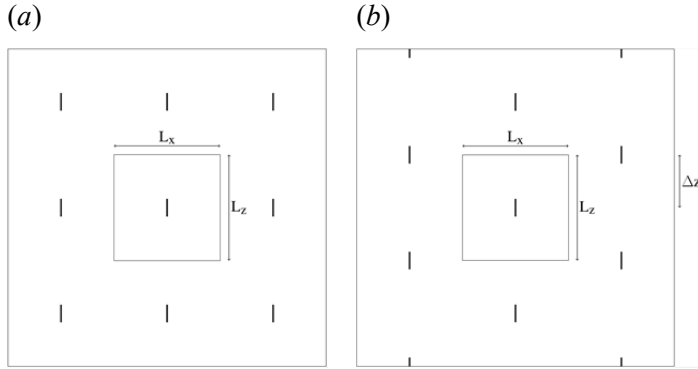


**Figure 2.** Schematic of array configurations: (a) aligned and (b) staggered ( $\Delta z = 0.5L_z$ ).

**Table 1.** Summary of flow conditions obtained from ‘empty box’ simulations

Roughness Height, $K_s$ [m]	Pressure Gradient [Pa/m]
0	$-6.43 \times 10^{-5}$
1	$-25.98 \times 10^{-5}$
5	$-37.88 \times 10^{-5}$

The top boundary of the domain is treated as a symmetry boundary, whereas the side boundaries are treated as periodic boundaries. Two different types of array configurations are examined, namely ‘aligned’ and ‘staggered’ configurations (Figure 2). For the aligned cases, the discs are fully aligned (spacing between neighbouring discs is 1 domain-length in both streamwise and spanwise directions, i.e.  $6D$ ,  $7D$  or  $14D$ ). For the staggered cases, the discs are arrayed in a fully staggered arrangement (spanwise displacement between two consecutive rows,  $\Delta z$ , is 0.5 domain-length, i.e.  $3D$ ,  $3.5D$  or  $7D$ ). The bottom boundary is treated as a wall with three different nominal roughness heights of  $K_s = 0\text{m}$ ,  $1\text{m}$  and  $5\text{m}$  (further details will be described later in Section 3.2 and in the Appendix).

To determine the streamwise pressure gradient across the computational domain (to be given as a boundary condition for the farm simulations), a preliminary ‘empty box’ simulation (i.e. setting the turbine resistance  $K = 0$ ) was performed for each of the three different roughness cases with a fixed mass flow rate yielding a cross-sectional average velocity of  $U_{av0} = 10\text{m/s}$ . The results of these ‘empty box’ simulations are summarised in Table 1. For all simulations, the density and viscosity of air are assumed to be  $\rho = 1.2\text{kg/m}^3$  and  $\mu = 1.8 \times 10^{-5}\text{kg/m-s}$ , respectively.

### 3.2. Computational methods

All computations, to solve numerically the 3D incompressible RANS equations, are performed using the commercial package ‘ANSYS FLUENT 16.2’ with its User Defined Functions (UDF) module for modifications. The Reynolds stress terms are modelled using the Standard  $k-\epsilon$  model of Launder and Spalding [10] and the numerical method used is nominally second-order accurate in space for pressure, momentum,  $k$  and  $\epsilon$  equations. The SIMPLE algorithm is used for pressure-velocity coupling.

The actuator disc is modelled as a stationary permeable disc (or porous disc) similarly to [11, 12] but with a local correction (or suppression) to the turbulent viscosity around the disc edge [8]. The loss of momentum in the streamwise ( $x$ ) direction (per unit disc area) is calculated as

$$M_x = K \cdot \frac{1}{2} \rho U_d^2 \quad (7)$$

where  $U_d$  is the local (rather than disc averaged) streamwise velocity through the disc. Since the disc-averaged thrust and power can be calculated as  $\int M_x dA$  and  $\int M_x U_d dA$ , respectively, the thrust and power coefficients of the disc are calculated as

$$C_T \equiv \frac{\text{Thrust}}{\frac{1}{2} \rho U_{F0}^2 A} = K \cdot \frac{\int U_d^2 dA}{U_{F0}^2 A} \quad (8)$$

and

$$C_P \equiv \frac{\text{Power}}{\frac{1}{2} \rho U_{F0}^3 A} = K \cdot \frac{\int U_d^3 dA}{U_{F0}^3 A} \quad (9)$$

For the disc resistance parameter  $K$ , two different values are used:  $K = 0.5$  and  $2$ , representing a low-resistance and high-resistance turbine, respectively. Note that  $K = 2$  is the theoretically optimal value for an isolated ideal turbine, regardless of whether the flow is sheared or not [9].

The effect of roughness of the bottom boundary (or ground) is modelled using a modified wall function for ‘fully rough’ walls available in ANSYS FLUENT 16.2. Specifically, the flow condition at the bottom boundary (for the cases with  $K_s = 1\text{m}$  and  $5\text{m}$ ) is determined based on the following wall function equations [13]:

$$\frac{U_p u^*}{\tau_w / \rho} = \frac{1}{\kappa} \ln \left( E \frac{\rho u^* y_p}{\mu} \right) - \Delta B \quad (10)$$

$$u^* = C_\mu^{0.25} k^{0.5}, \quad \Delta B = \frac{1}{\kappa} \ln(1 + C_s K_s^+) \quad (11a,b)$$

$$K_s^+ = \frac{\rho K_s u^*}{u_\tau}, \quad u_\tau = \sqrt{\frac{\tau_w}{\rho}} \quad (12a,b)$$

where  $U_p$  is the velocity at the centroid of the wall-adjacent cell (i.e. at  $y = y_p$ ),  $\kappa = 0.4187$  and  $E = 9.793$  are the von Karman constant and an empirical constant used in ANSYS FLUENT, respectively,  $C_\mu = 0.09$  is the eddy viscosity constant used in the Standard  $k$ - $\epsilon$  model, and  $C_s = 0.5$  is the roughness constant used in this study. It should be noted that the nominal roughness height  $K_s$  used in this study is for ‘sand-grain’ type roughness (often used in engineering flow problems) but this is related to the aerodynamic roughness parameter  $y_0$  (or ‘ $z_0$ ’ often used in ABL flow problems) as  $K_s = (E/C_s)y_0$  [14]. Therefore, the three different roughness heights considered in this study,  $K_s = 0\text{m}$ ,  $1\text{m}$  and  $5\text{m}$ , correspond to  $y_0 = 0\text{m}$ ,  $0.051\text{m}$  and  $0.255\text{m}$ , respectively. Traditionally, this wall roughness model in ANSYS FLUENT had a limitation that the distance from the wall to the centroid of the wall-adjacent cell needed to be greater than the roughness height  $K_s$ , which often caused difficulties in applying this model to ABL flow problems [14]. However, this limitation has been overcome in recent versions of ANSYS FLUENT by employing a remedial approach called ‘virtually shifting the wall’ [13], which, when the non-dimensional roughness height  $K_s^+$  is in the ‘fully rough’ regime ( $K_s^+ \geq 90$ ), allows to virtually shift the wall by 50% of the roughness height, i.e.

$$y_{p(\text{corrected})}^+ = y_{p(\text{original})}^+ + \frac{K_s^+}{2} \quad (13)$$

This virtual wall shifting is justified on the assumption that roughness elements create a ‘blockage’ of approximately 50% of the roughness height [13]. This approach makes it possible to use a fine mesh near a rough wall with a large  $K_s$  value; therefore a sufficiently fine mesh designed for the case with  $K_s = 0\text{m}$  (to be described in detail in Section 3.3) can be used for  $K_s = 1\text{m}$  and  $5\text{m}$  as well without modifications. A validation study is presented in the Appendix to confirm that the wall shear stress  $\tau_w$  calculated using the above model is insensitive to the size of wall-adjacent cells.

All simulations are steady-state simulations and they are run for a very large number of iterations (approximately one million) until residuals and key variables, such as the bottom shear stress, are fully converged. This large number of iterations (to obtain a fully converged solution) is required due to the use of doubly periodic boundary conditions. Figure 3 shows examples of the convergence of spatially averaged bottom shear stress,  $\langle \tau_w \rangle$ , and the streamwise velocity averaged over the disc area,  $U_T$ .

### 3.3. Computational grids

Multi-block structured grids with hexahedral cells are used for all simulations. A 2D (cross-sectional) mesh is created first at one of the vertical ( $y$ - $z$ ) planes in the domain. This mesh has a minimum grid spacing of  $0.01D$  inside and around the disc, and  $0.001D$  above the bottom boundary (Figure 4a). This 2D mesh is then extruded in the streamwise ( $x$ ) direction to create the final 3D mesh. For different domain sizes, the same 2D mesh around the disc is used as a base but with increasing the horizontal dimension before performing the streamwise extrusion. For the streamwise direction, a uniform grid spacing of  $0.01D$  is used between  $x = -0.1D$  and  $0.5D$ , with the disc located at  $x = 0$ , and allowing a

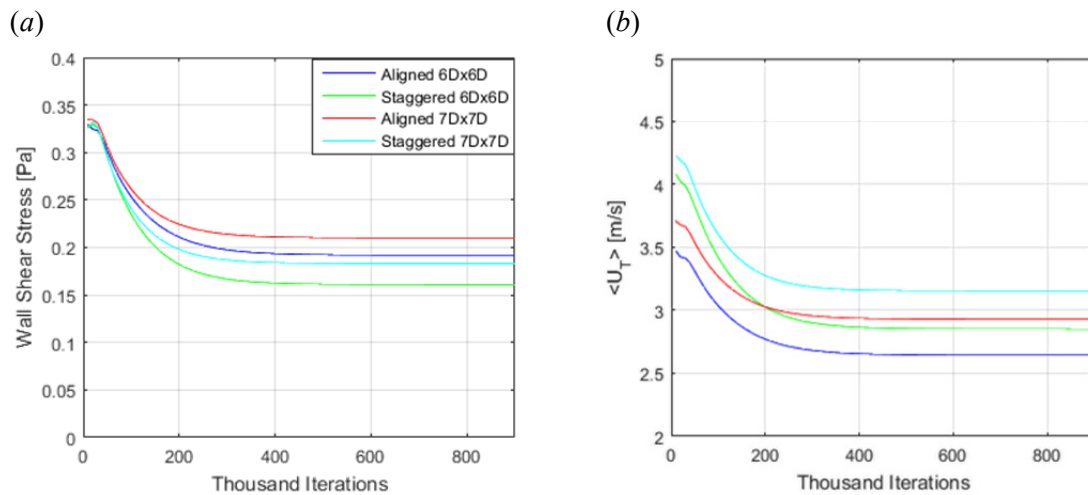


**Figure 3.** Examples of the convergence of solutions (for 4 cases with  $K_s = 5m$  and  $K = 2$ ): (a) horizontally averaged bottom shear stress  $\langle \tau_w \rangle$ ; and (b) disc-averaged streamwise velocity  $U_T$ .

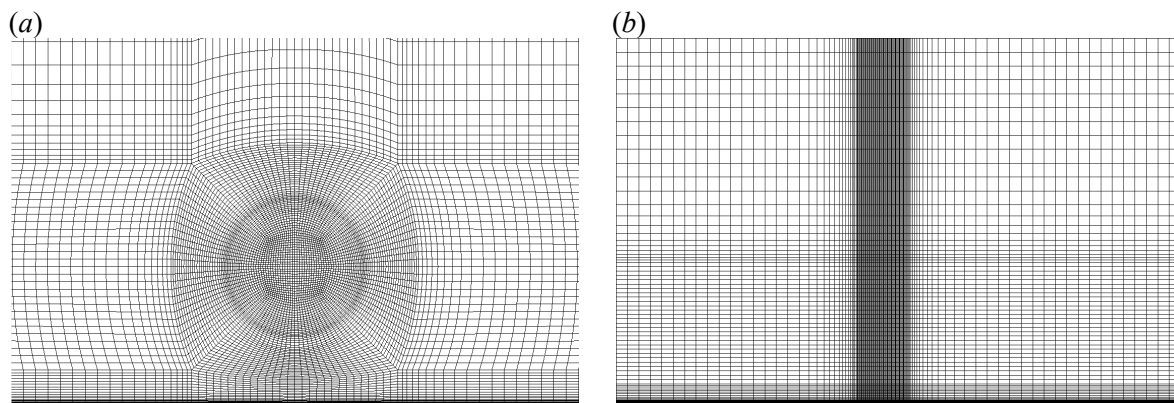


**Figure 4.** Computational mesh: (a) cross-sectional view around the disc ( $y$ - $z$  plane); and (b) lateral view ( $x$ - $y$  plane).

larger spacing outside this region, with a maximum spacing of approximately  $0.15D$  (Figure 4b). This methodology ensures that all simulations are performed with the same high-quality mesh around the disc and near the bottom boundary. The total number of cells for the 3D domains varies between  $1.64 \times 10^6$  for the  $6D \times 6D$  case and  $3.13 \times 10^6$  for the  $14D \times 14D$  case.

### 3.4. Results

Figure 5 shows the ‘natural’ boundary layer profiles (streamwise velocity and turbulent kinetic energy or TKE) obtained with no disc resistance ( $K = 0$ ) for the three different ground roughness cases. Note that, although not presented here, these ‘natural’ profiles are horizontally homogeneous across the entire domain due to the periodic boundary conditions. As explained in Section 3.1, these ‘empty box’ simulations are used to determine the ‘natural’ pressure gradient (to be used in the farm simulations with non-zero  $K$  values) as summarised in Table 1. Also, as described in Section 2.1, these ‘natural’ boundary layer profiles can be used to calculate parameters for comparison with the Nishino model, such as the farm-layer height ( $H_F$ ), the natural farm-layer wind speed ( $U_{F0}$ ) and the natural bottom shear stress ( $\tau_{w0}$ ). The farm-layer height, defined by Equation (2), was found to be  $H_F = 2.6D$  for all three different roughness cases in this study.

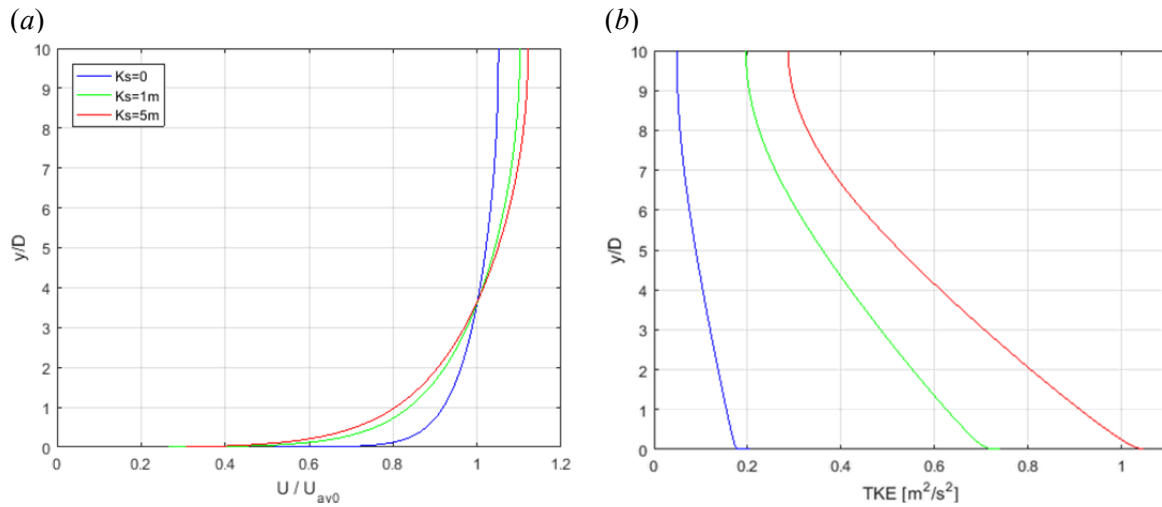


**Figure 5.** Boundary layer profiles for the ‘natural’ ( $K = 0$ ) cases with three different bottom roughness heights: (a) streamwise velocity; and (b) turbulent kinetic energy.

**Table 2.** Summary of computational results for  $K_s = 0\text{ m}$  ( $U_{F0} = 9.18\text{ m/s}$ ,  $\tau_{w0} = 0.0643\text{ Pa}$ )

Configuration	$\lambda/C_{f0}$	$K$	$\alpha$	$\beta$	$C_T$	$C_P$	$\tau_w/\tau_{w0}$	$\gamma$
Aligned, $6D \times 6D$	17.5	2	0.503	0.307	0.0478	0.0074	0.165	1.53
Aligned, $7D \times 7D$	12.9	2	0.520	0.341	0.0631	0.0112	0.191	1.54
Staggered, $6D \times 6D$	17.5	2	0.641	0.247	0.0503	0.0080	0.120	1.52
Staggered, $7D \times 7D$	12.9	2	0.637	0.286	0.0666	0.0122	0.144	1.55

**Table 3.** Summary of computational results for  $K_s = 1\text{ m}$  ( $U_{F0} = 8.34\text{ m/s}$ ,  $\tau_{w0} = 0.2597\text{ Pa}$ )

Configuration	$\lambda/C_{f0}$	$K$	$\alpha$	$\beta$	$C_T$	$C_P$	$\tau_w/\tau_{w0}$	$\gamma$
Aligned, $6D \times 6D$	3.58	2	0.517	0.551	0.163	0.0466	0.417	1.47
Aligned, $7D \times 7D$	2.63	2	0.537	0.595	0.205	0.0655	0.463	1.48
Staggered, $6D \times 6D$	3.58	2	0.644	0.472	0.185	0.0564	0.337	1.45
Staggered, $7D \times 7D$	2.63	2	0.646	0.527	0.233	0.0794	0.389	1.48
Staggered, $14D \times 14D$	0.66	2	0.642	0.778	0.499	0.250	0.673	1.58
Staggered, $6D \times 6D$	3.58	0.5	0.866	0.626	0.147	0.0799	0.473	1.60
Staggered, $7D \times 7D$	2.63	0.5	0.869	0.681	0.175	0.104	0.539	1.61
Staggered, $14D \times 14D$	0.66	0.5	0.872	0.878	0.293	0.225	0.808	1.64

**Table 4.** Summary of computational results for  $K_s = 5\text{ m}$  ( $U_{F0} = 8.01\text{ m/s}$ ,  $\tau_{w0} = 0.3787\text{ Pa}$ )

Configuration	$\lambda/C_{f0}$	$K$	$\alpha$	$\beta$	$C_T$	$C_P$	$\tau_w/\tau_{w0}$	$\gamma$
Aligned, $6D \times 6D$	2.26	2	0.525	0.628	0.218	0.0722	0.507	1.46
Aligned, $7D \times 7D$	1.66	2	0.546	0.670	0.268	0.0982	0.555	1.47
Staggered, $6D \times 6D$	2.26	2	0.649	0.549	0.254	0.0904	0.425	1.43
Staggered, $7D \times 7D$	1.66	2	0.649	0.607	0.310	0.123	0.484	1.45
Staggered, $14D \times 14D$	0.42	2	0.649	0.834	0.587	0.318	0.756	1.54
Staggered, $6D \times 6D$	2.26	0.5	0.867	0.708	0.189	0.116	0.572	1.62
Staggered, $7D \times 7D$	1.66	0.5	0.872	0.757	0.218	0.144	0.638	1.61
Staggered, $14D \times 14D$	0.42	0.5	0.876	0.916	0.322	0.259	0.866	1.64

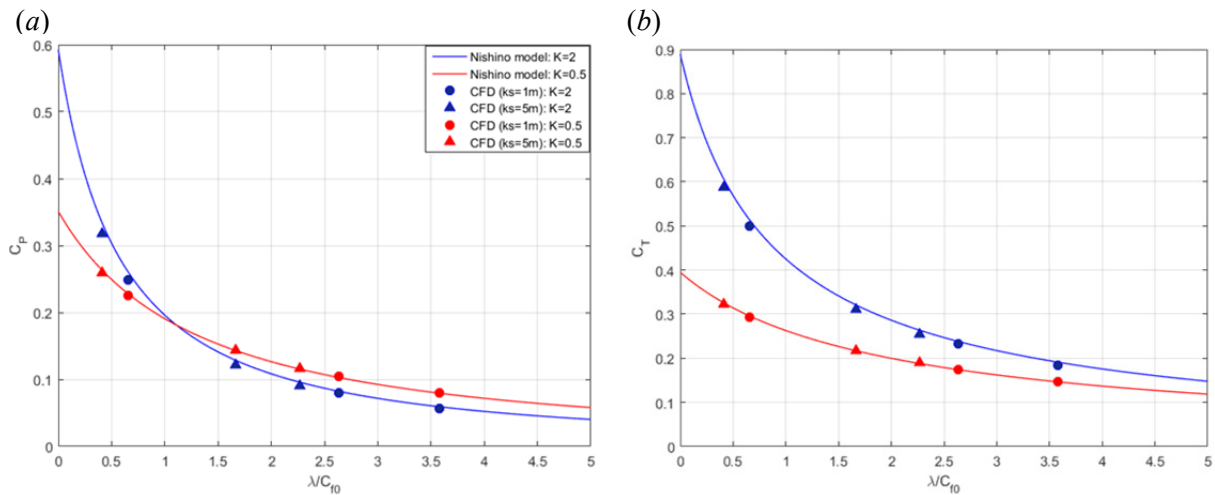


**Figure 6.** Comparisons between the 3D RANS simulations of staggered arrays and the Nishino model predictions (with  $\gamma = 1.5$ ): (a) power coefficient; and (b) thrust coefficient.

Once these ‘empty box’ simulations have been conducted, it is possible to run the farm simulations (i.e. pressure-driven boundary layer simulations with non-zero  $K$  values) and calculate the parameters described in the Nishino model, such as  $\alpha$ ,  $\beta$ ,  $C_T$ ,  $C_p$  and  $\gamma$ , to evaluate the farm performance. The results are summarised in Tables 2, 3 and 4 for all scenarios investigated in this study, i.e. for three different roughness heights, three different domain sizes, two different array configurations (aligned and staggered) and two different disc resistance values. Note that the (normalised) farm density  $\lambda/C_{f0}$  depends only on the roughness height and domain size and is therefore already known before running the farm simulations. Of particular interest is that the values of  $\gamma$  obtained from the farm simulations performed in this study are all around 1.5 to 1.6. This agrees with the prediction made by Nishino [8] that the value of  $\gamma$  should be less than 2 for ‘real’ arrays (such as the ‘aligned’ and ‘staggered’ arrays considered here) and also suggests that this parameter  $\gamma$  (which is the only empirical parameter in the model) can be calibrated relatively easily for a wide range of practical array configurations.

Figure 6 shows a comparison between the farm simulations of ‘staggered’ arrays and the Nishino model [8] for the power coefficient  $C_p$  and thrust coefficient  $C_T$ . Note that  $\gamma = 1.5$  has been employed in the Nishino model for this comparison. As can be seen from the figure, the agreement is excellent for both high and low disc resistance cases ( $K = 2$  and  $0.5$ ). This shows the usefulness of the Nishino model not only for providing an upper limit to the performance of ‘ideal’ arrays (as described in [8]) but also for predicting the performance of ‘staggered’ arrays with wide ranges of  $K$  and  $\lambda/C_{f0}$  values. Most importantly, both simulations and theoretical predictions show a clear tendency that the optimal turbine resistance is smaller in a ‘dense’ wind farm than in a ‘sparse’ wind farm, i.e. low-resistance turbines (with  $K = 0.5$  in this example) perform better than high-resistance turbines (with  $K = 2$  in this example) when the normalised farm density  $\lambda/C_{f0}$  is large.

Although not presented in Figure 6, the simulations of ‘aligned’ arrays tend to give approximately 10% to 20% lower  $C_p$  values compared to the ‘staggered’ array simulations (see Tables 2, 3 and 4) and the Nishino model. To predict the performance of such ‘less efficient’ arrays accurately, the negative effect of turbine wake interaction would need to be taken into account in the theoretical model.

#### 4. Concluding remarks

The results of 3D RANS simulations of ‘infinitely large’ wind farms presented above show that the simple 1D theoretical wind farm model proposed by Nishino [8] can be a good first approximation to the solution of this apparently complex 3D flow problem. In particular, it has been shown that the power coefficient of a number of ideal turbines (or actuator discs) arranged in a ‘staggered’ manner

can be predicted very well as a function of the turbine resistance  $K$  and the normalised farm density  $\lambda/C_{f0}$  by adjusting the only empirical parameter  $\gamma$  in the theoretical model. It has also been shown that the value of  $\gamma$  should be approximately 1.5 for all scenarios considered in this study. It should be noted that, although the 3D RANS simulations performed in this study rely on the Standard  $k$ - $\varepsilon$  turbulence model (with a local modification around the disc edge) and therefore the results are not as realistic as LES (for example) in terms of the details of turbulent mixing behind the disc, the simulations have been performed with care regarding the mesh quality and convergence to obtain sufficiently accurate numerical solutions of the governing equations. The excellent agreement between the 3D simulation results (for ‘staggered’ arrays) and the 1D theoretical model shown earlier in Figure 6 suggests the usefulness of the 1D theoretical model. As an example of how the theoretical model can be useful, it has also been shown that the optimal turbine resistance can be predicted easily as a function of the normalised farm density (and this prediction seems almost as accurate as what can be made using 3D RANS simulations). This analysis could be extended further in future studies to explore, for example, an optimal turbine rotor design as a function of the normalised farm density.

Although all simulation results presented in this paper suggest that the theoretical farm model is promising, there are still many important issues to be addressed in future studies. For example, the size and ‘hub-height’ of the rotors (relative to the thickness of the ABL) have been fixed for all scenarios in this study; these geometrical parameters, however, may affect the value of  $\gamma$  in the theoretical model. Another physical factor that may affect the value of  $\gamma$  is the stability of the ABL. Hence a more comprehensive set of numerical simulations would be necessary to calibrate the empirical parameter  $\gamma$  in the theoretical model for a wider range of problems. Apart from the calibration of  $\gamma$ , it would also be important to further examine the validity of using the classical actuator disc theory as the local-scale flow model in this two-scale coupled wind farm model. The present study has shown that this approach works well for ‘fully staggered’ arrays with a range of inter-disc spacing (from  $6D$  to  $14D$ ); however this would not be the case when the inter-disc spacing is much smaller and there are strong (usually negative) interactions of individual turbine wakes. For such dense wind farms, some sort of corrections to the local-scale flow model would be required to account for the effect of turbine wake interactions. In addition, another type of correction to account for the influence of farm size would be necessary for the theoretical model to be applied to real (not ‘infinitely’ large) wind farms. Finally, but not least, the present study employs the assumption that the flow over the farm is driven by a constant streamwise pressure gradient; this is a commonly used assumption but not the case in the real world (as discussed in e.g. [6]). Most of these issues are currently under investigation.

## Acknowledgments

Part of this study was conducted as part of the MULTI-WIND (integrated multi-scale modelling for optimal wind energy extraction) project, funded by EPSRC through the Institutional Sponsorship Fund allocated to Cranfield University (EP/P511134/1).

## Appendix

As mentioned in Section 3.2, in this study we have used the ‘sand-grain’ type wall roughness model available in ANSYS FLUENT 16.2 to simulate the effect of bottom (ground) roughness. In order to use this approach, the near-wall flow must be in the ‘fully rough’ regime. This condition is satisfied if  $K_s^+ \geq 90$ . Blocken et al. [14] noted that in most cases, an ABL flow is in this ‘fully rough’ regime as the roughness is usually large enough to neglect the viscous sublayer. This is the case in the present study as well; it has been confirmed that  $K_s^+ \geq 90$  in all simulations with  $K_s = 1\text{m}$  and  $5\text{m}$ .

To confirm that the wall shear stress calculated using this wall function approach is insensitive to the size of wall-adjacent cells, we performed (separately from the farm simulations presented in the main part of this paper) a set of 2D RANS simulations of boundary layer flows. A short and tall 2D domain of  $(L_x, L_y) = (100\text{m}, 1000\text{m})$  was employed with streamwise ( $x$ ) periodic boundary conditions. Four different near-wall grid resolutions ( $0.001\text{m}$ ,  $0.01\text{m}$ ,  $0.1\text{m}$  and  $1\text{m}$ ) and seven different roughness heights ( $k_s = 0.005\text{m}$ ,  $0.01\text{m}$ ,  $0.05\text{m}$ ,  $0.1\text{m}$ ,  $0.5\text{m}$ ,  $1\text{m}$  and  $5\text{m}$ ) were considered, leading to 28 different

simulation cases. Note that some of these cases are designed such that the size of wall-adjacent cells is larger than the roughness height, whereas the other cases are not. Figure 7 summarises the results of bottom shear stress obtained in these 2D boundary layer simulations. As can be seen from the figure, the sensitivity of the bottom shear stress to the wall-adjacent cell size is low. This supports the validity of the roughness modelling approach employed in the farm simulations in this study.

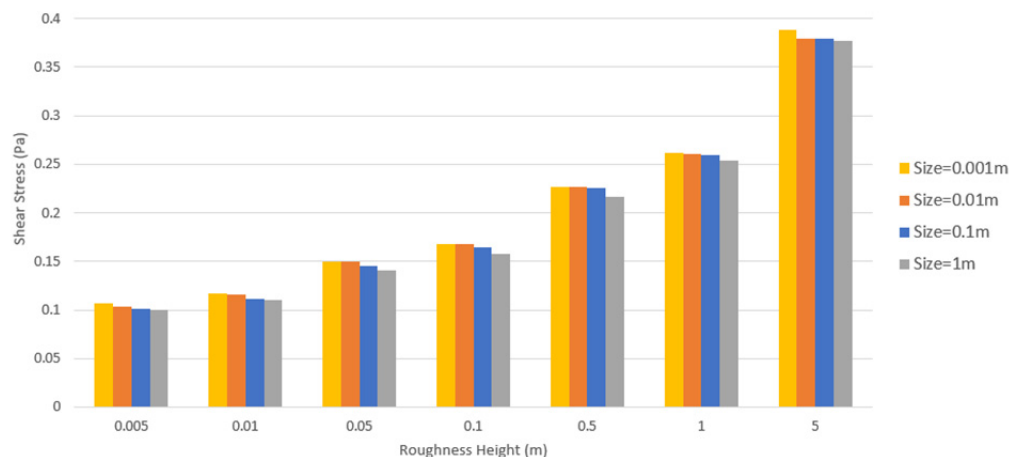


**Figure 7.** Sensitivity of the bottom shear stress to the size of wall-adjacent cells in 2D periodic boundary layer simulations (for seven different roughness heights).

## References

- [1] Frandsen S, Barthelmie R, Pryor S, Rathmann O, Larsen S, Højstrup J and Thøgersen M 2006 Analytical modelling of wind speed deficit in large offshore wind farms *Wind Energ.* **9** 39-53
- [2] Frandsen S 1992 On the wind speed reduction in the center of large clusters of wind turbines *J Wind Eng. Ind. Aerodyn.* **39** 251-265
- [3] Emeis S and Frandsen S 1993 Reduction of horizontal wind speed in a boundary layer with obstacles *Bound.-Layer Meteor.* **64** 297-305
- [4] Emeis S 2010 A simple analytical wind park model considering atmospheric stability *Wind Energ.* **13** 459-469
- [5] Emeis S 2012 *Wind Energy Meteorology: Atmospheric Physics for Wind Power Generation* (Berlin, Heidelberg: Springer) chapter 6
- [6] Calaf M, Meneveau C and Meyers J 2010 Large eddy simulation study of fully developed wind-turbine array boundary layers *Phys. Fluids* **22** 015110
- [7] Meneveau C 2012 The top-down model of wind farm boundary layers and its applications *J Turbul.* **13** N7
- [8] Nishino T 2016 Two-scale momentum theory for very large wind farms *J. Phys.: Conf. Ser.* **753** (TORQUE 2016, Munich, Germany) 032054
- [9] Draper S, Nishino T, Adcock T A A and Taylor P H 2016 Performance of an ideal turbine in an inviscid shear flow *J. Fluid Mech.* **796** 86-112
- [10] Launder B E and Spalding D B 1974 The numerical computation of turbulent flows *Comput. Methods Appl. Mech. Eng.* **3** 269-289
- [11] Nishino T and Willden R H J 2012 Effects of 3-D channel blockage and turbulent wake mixing on the limit of power extraction by tidal turbines *Int. J. Heat Fluid Flow* **37** 123-135
- [12] Nishino T and Willden R H J 2013 Two-scale dynamics of flow past a partial cross-stream array of tidal turbines *J. Fluid Mech.* **730** 220-244
- [13] ANSYS Inc. 2015 ANSYS Fluent User's Guide, Release 16.2
- [14] Blocken B, Stathopoulos T and Carmeliet J 2007 CFD simulation of the atmospheric boundary layer: wall function problems *Atmospheric Environment* **41(2)** 238-252